INT. J. REMOTE SENSING, 1994, VOL. 15, NO. 5, 979–1008

# The problem of AVHRR image navigation revisited

V. M. KRASNOPOLSKY

General Sciences Corporation, 6100 Chevy Chase Drive, Laurel, MD 20707, U.S.A.

and L. C. BREAKER

NOAA, National Meteorological Center, Washington, DC 20233, U.S.A.

*(Received 28 December 1992; in final form 15 June 1993)*

**Abstract.** In this study, Earth location errors in AVHRR satellite data and methods for their correction are examined with particular application to oceanic regions far removed from ground control. A general correction procedure, using landmarks or Ground Control Points (GCPs) and taking into account landmark uncertainties, is presented. Correction functions are derived as expansions for any complete basis. Operationally-available estimates of Earth location are used as a first-guess in developing the correction procedure. In particular, polynomial expansions are used to represent the correction functions which provide the basis for renavigating the satellite data. The coefficients of the polynomial expansions are obtained using the method of least-squares. The stability of the correction procedure with respect to local errors in navigation, (i.e. within a scene) and how to select the correct order of the correction polynomials are examined. Uncertainty in extrapolating navigation corrections over remote regions is examined and quantified. The importance of landmark uncertainty in degrading renavigation accuracy is also addressed. Several parameters are introduced to optimize the choice of GCPs and their distributions. The procedures which are developed are then applied to simulated and actual AVHRR imagery. Finally, the impact of local errors in navigation, which most likely arise from rapid variations in spacecraft attitude, on renavigation accuracy is emphasized and one possible solution proposed.

## 1. Introduction

The Advanced Very High Resolution Radiometer (AVHRR) is a high-resolution, multi-channel scanning radiometer that has been flown aboard NOAA's TIROS-N polar-orbiting satellites since 1978. Satellite imagery from this instrument has been used extensively to study a variety of oceanic features based on their thermal manifestations at the surface. As the oceanographic applications for AVHRR data have become more sophisticated, the need for greater Earth location accuracy has likewise increased. For example, by measuring the displacements experienced by selected thermal features between successive images, it is often possible to infer the apparent advective motion that transports these features. Such feature-tracking methods place stringent requirements on Earth location accuracy since the associated displacements may not be large compared to the uncertainties in the navigation. Although careful co-registration of successive images in coastal regions usually produces close alignment near coastlines which are often used as a common reference in the co-registration process, there is no guarantee that close alignment

will occur between the images for oceanic locations far-removed from land. Thus, we are motivated to reexamine the question of Earth location accuracy as new applications for AVHRR satellite imagery arise which continue to place greater reliance on earth location accuracy.

In navigating AVHRR satellite data, two basic approaches are used. The first employs an ephemeris model to predict the orbital elements which are then used to calculate Earth locations for the satellite data; the second involves the use of landmarks that provide a basis for relocating AVHRR image pixels which are usually first navigated approximately using an ephemeris model (e.g., Emery *et al.* 1989). Our primary interest in this study involves the use of landmarks, and a number of issues arise in their use that significantly influence the quality of the renavigated data. They include the number and distribution of landmarks, landmark uncertainty, and the mathematical procedures that are used to relocate the satellite data. These issues are examined in some detail.

Since the mid-1970s, a number of studies has addressed the problem of navigation for data acquired from polar-orbiting satellites. The various types of geometric errors and methods for their correction for Landsat data were outlined by Bernstein and Ferneyhough (1975). Malhotra and Rader (1975) described the two basic approaches for Earth-locating remotely-sensed data using (1) an ephemeris model to determine the orbital position and attitude of a spacecraft as a function of time, and (2), landmarks or Ground Control Points (GCPs) as known reference points on the Earth's surface as a basis for relocating the entire field of image elements or pixels. Legeckis and Pritchard (1976) developed an algorithm to correct satellite data from the Very High Resolution Radiometer (VHRR) for geometric distortions due to Earth curvature, Earth rotation and rolling motions of the spacecraft. A method for assigning geographical coordinates to digital satellite imagery from the VHRR was given by Kirkham and Stevenson (1976). McConaghy (1980) presented a technique for analytically determining the geographic location of individual pixels in VHRR satellite data to an accuracy of 0·1° or less, in latitude and longitude.

According to Clark and LaViolette (1981), AVHRR data from TIROS-N could be reliably registered on to a geographical grid using two-dimensional, third-order polynomials. The remapped data were useful for tracking the movements of oceanic fronts. Freidman *et al.* (1983) were able to reduce the computational effort involved in obtaining precise geometric corrections for Landsat data by reducing the required number of GCPs from an average of 15 to 4, through (1) the processing of multiple scenes, and (2), physically modelling the motions of the spacecraft. Two methods for geometrically correcting AVHRR data were compared by Emery and Ikeda (1984). One method included Earth oblateness and the second assumed a circular orbit for the satellite. Both methods used GCPs as a final step in the Earth location process. Significantly fewer GCPs were required to achieve a specified degree of Earth location accuracy for the case where Earth oblateness was included. Brunel and Marsouin (1987) presented a method for navigating AVHRR data in real time based on an extrapolation of the satellite's orbital elements which were calculated from the ARGOS Data Collection and Location System. The mean navigational error using this method was 4·7 km. Cracknell and Paithoonwattanakij (1989) were apparently able to achieve subpixel accuracy in renavigating AVHRR data by combining AVHRR and Landsat images using the method of Torlegard (1986). The NOAA/

TBUS mean orbital elements were used by Kloster (1989) in an orbital prediction model as a basis for Earth locating AVHRR data.

A comprehensive review of the methods used in AVHRR image navigation was given by Emery *et al.* (1989). A procedure for automatically navigating AVHRR image data using both ARGOS and TBUS orbital elements and an operational ephermeris model was developed by Marsouin and Brunel (1991). O'Brien and Turner (1992) applied an efficient template-matching algorithm to raw AVHRR image data to automatically identify coastal features to be used as GCPs for image registration and to provide local corrections for the Earth locations predicted from the TBUS orbital elements. Gupta (1992) used matching GCPs in slave and master images to obtain acceptable geometric co-registration. Deviations in geometric registration related to the distributions of GCPs were also examined. Bordes *et al.* (1992) applied template-matching between selected coastal landmarks in AVHRR images with corresponding landmarks taken from a digital coastline reference file. Accuracy of the mapped AVHRR data using this technique was on the order of one pixel.

The text proceeds as follows. First, various sources of Earth location error for AVHRR satellite data and examples of errors in Earth location are given. A technique for correcting Earth location errors is presented next; the uncertainties that arise in landmark location and in the extrapolation of the corrections over remote regions are included. Results of the correction technique which is developed are presented followed by a discussion and a summary with recommendations.

## 2. Earth location errors

### 2.1. *Sources of error in Earth location*

To find the exact Earth location of each picture element (pixel) in a satellite image, the following information is required:

1. *Orbital elements*: semi-major axis, eccentricity, right ascension of the orbital plane, inclination of the orbital plane, argument of perigee, and the angular position of the spacecraft within its orbital plane. These elements determine the satellite's position in space with respect to the earth as a function of time.
2. *Attitude*: roll, pitch and yaw, which determine the orientation of the satellite as a function of time.
3. *Sensor geometry*: determines the viewing angle of the sensor as a function of time.

Because the models that are used to predict the orbital elements contain various sources of error, predictions based on these models can only be taken as approximate. Table 1 below shows several sources of Earth location error plus rough estimates of their magnitudes (for additional information see Emery *et al.* 1989, Bordes *et al.* 1992).

Figure 1 shows spacecraft attitude time histories for roll, pitch and yaw for one orbit of the NOAA-11 polar-orbiting satellite. Although variations in roll and pitch are small (absolute value $\leqslant 0{\cdot}03°$), yaw is significant in this case ($\leqslant -0{\cdot}4°$) leading to maximum Earth location errors of roughly 10 km toward the edges of the scan. Although these data may not be representative, they emphasize the importance of variations in yaw as a likely contributor to errors in Earth location.

Table 1. A partial list of the sources of error in Earth location for AVHRR satellite data.

| Error source | Direction ($x$ = along-scan, $y$ = along-track) | Estimated magnitude (km) | Comments |
|---|---|---|---|
| Orbital elements | $x$ and $y$ | $\sim 10$ | (1) Orbit ellipticity<br>(2) Oblateness of the Earth<br>(3) Local variations of gravity<br>(4) Solar activity |
| Timing errors* | $y$ | $\sim 2$ | Affects only along-track direction |
| Yaw† | $x$ and $y$ | $\leqslant 3$ | |
| Pitch | $y$ | $\leqslant 1$ | |
| Roll | $x$ | $\leqslant 1$ | |
| Interpolation of bench-mark locations | $x$ and $y$ | $\sim 1$ | Remapping from ephemeris output |
| Imperfect registration between channels | $x$ and $y$ | $\leqslant 1$ | |
| Lowered resolution due to scan angle dependence‡ | $x$ and $y$ | $\leqslant 6$ | Only significant at high zenith angles |

*Timing errors are due to the clock drift aboard the satellite. Corrections for clock drift are applied when the accumulated drift has reached values usually in the range of 0·5 to 1·0 seconds. As a result, we have selected a value for clock drift of 300 m sec$^{-1}$ as representative which corresponds to an Earth location error of approximately 2 km (D. Solomon, personal communciation).

†Values of 0·03° for the error in roll and pitch and 0·1° for yaw, were used to estimate the corresponding errors in earth location (D. Solomon, personal communication).

‡The navigation error due to scan angle dependence corresponds to approximately half the distance or range of uncertainty between adjacent pixels in the alongscan direction at the edge of the scan.

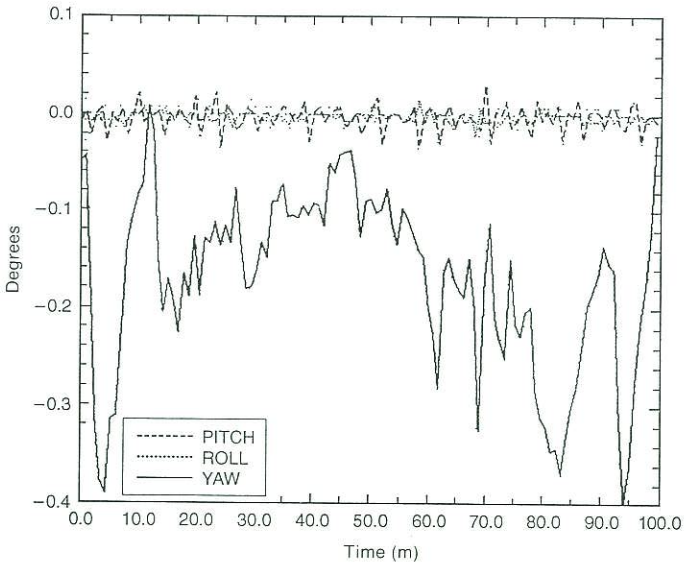


Figure 1. Roll, pitch and yaw for one orbit of the NOAA-11 spacecraft. The date is 24 March 1992.

Consequently, we give a brief description of how yaw is measured aboard the spacecraft. Yaw is measured in two modes, the nominal mode and the YGC (yaw gyroscope compassing) mode. The nominal or primary operating mode relies on periodic Sun angle measurements to reset the gyroscopic sensor which measures yaw aboard the spacecraft once each orbit. The secondary or YGC mode is used when Sun angle measurements cannot be made, a problem which often arises during the winter. As a result, the accuracy of yaw measurements in the YGC mode is reduced (J. Shepherd, personal communciation).

### 2.2. *Classification of errors*

One method of classifying errors in Earth location is according to their frequency of variation (e.g., Friedmann *et al.* 1983):

1. *Low frequency errors*: when the periods of the error variations are much greater than the scene imaging time. Unpredictable orbital variations contribute to low frequency errors.
2. *High frequency errors*: when the error variations occur over periods of the order of, or less than, the scene imaging time ($\approx 5$ minutes for the AVHRR). Spacecraft motions (i.e., roll, pitch and yaw) contribute to high frequency errors.

Low frequency errors are essentially constant over the scene (they also have low spatial frequency) and often require only a constant shift in the image coordinates to provide an adequate correction (e.g., Bordes *et al.* 1992). High frequency errors may vary significantly within a scene and are inherently more difficult to correct.

These distinctions are important because they reflect different components of the error generation process, components which often have different physical origins.

### 2.3. *Examples of errors in Earth location*

The space and time scales associated with Earth location errors for AVHRR satellite data have not been examined extensively. (The few published figures on navigation accuracy vary from subpixel to several pixels or more for AVHRR satellite imagery which has been renavigated using landmarks (e.g., and RMS error of 1·5 km was quoted by Cornillon *et al.* 1986)). As a result, we present several examples of earth location error for two geographic regions (in this section and in § 4) based on navigation data provided by NOAA/NESDIS. However, the extent to which these errors are representative is not known.

Initially, we consider a sequence of eight AVHRR images acquired over the Persian Gulf from 2–15 August 1991 for NOAA-11. The resolution of these images is 2·2 km. Fifteen GCPs were chosen over this region.

Figure 2 shows the variation in the apparent location of one selected GCP over the sequence of eight images. The smaller rectangles represent estimated landmark uncertainties which reflect our inability to select the exact location or pixel of interest. The outer rectangle brackets these locations and is roughly 20 km (longitude) × 8 km (latitude).

Figure 3 shows the space and time variation in Earth location error for nine landmarks over the sequence. A tendency for the resultant errors to be greatest in the alongscan direction is clearly indicated in this case. The Earth location errors vary from image to image with an overall RMS value of 5·4 km.

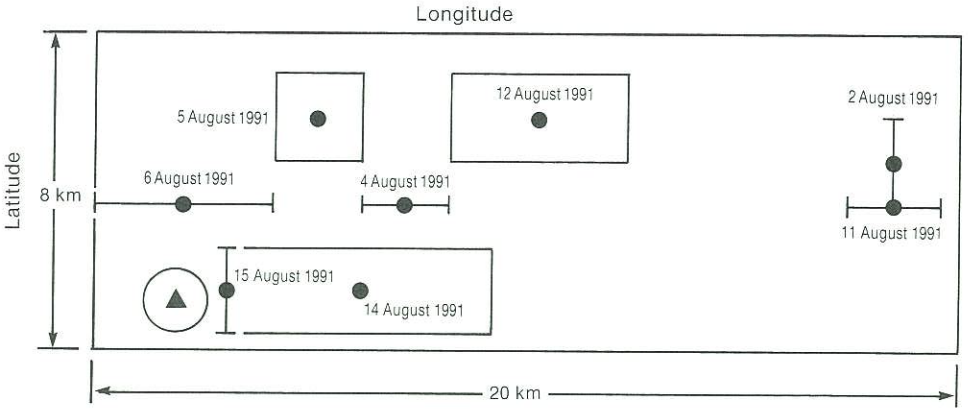


Figure 2. Apparent locations (black dots) of one selected GCP in the Persian Gulf area for a sequence of eight images. The smaller rectangles (or bars) represent estimated landmark uncertainties. The black triangle represents the 'true' location of the GCP taken from a map (National Geographic Society, Middle East; scale 1:5 877 000), and the circle represents our estimate of map uncertainty. Numbers near the dots indicate day/month/year.

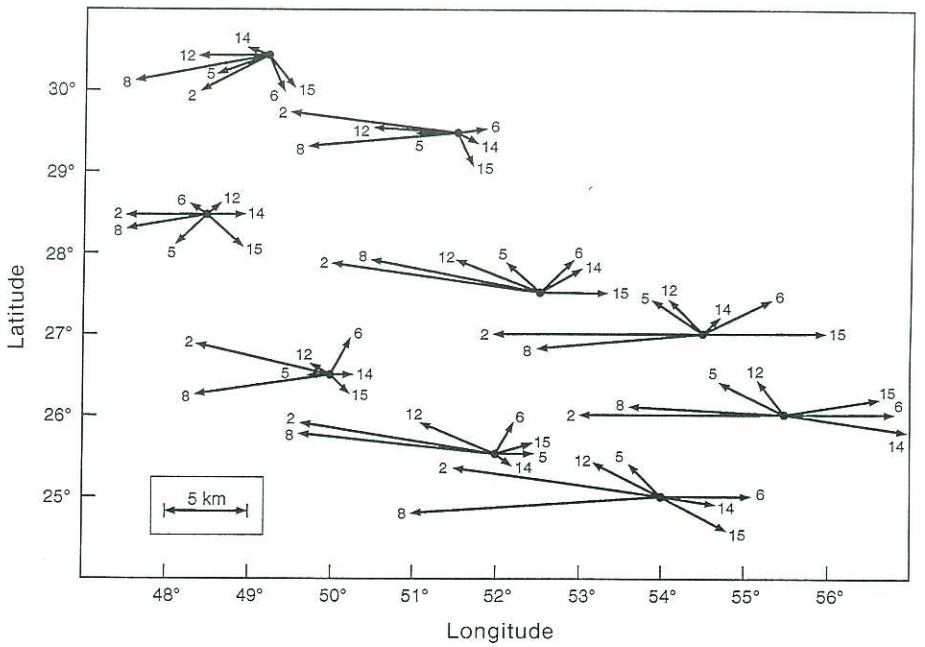


Figure 3. Space and time variation of Earth location errors for nine landmarks around the Persian Gulf for a sequence of seven images. Numbers at the arrow heads indicate the corresponding dates during August 1991.

In a second case, an image was acquired over the Gulf of Mexico from 25 May 1992 from NOAA-11 (this example is included in § 4); the RMS error in this case was 15·5 km (figure 8). The magnitudes and directions of these errors appear to be rather consistent throughout the scene, in contrast to the greater variability indicated for the Persian Gulf case. In general, these errors are expected to be both location and time dependent.

The Earth location error statistics for the sequence of eight images over the Persian Gulf are shown in table 2 together with similar statistics from Marsouin and Brunel (1991) for AVHRR data obtained from NOAA-9 and NOAA-10, and from Bordes *et al.* (1992) for NOAA-11. The results of Marsouin and Brunel (1991) were obtained for 16 images from 19 June to 26 September 1988 and those for Bordes *et al.* (1992) from a larger set of images acquired between May and November 1990.

There are considerable differences in the results obtained by Marsouin and Brunel (1991), by Bordes *et al.* (1992) and those obtained by us. These differences emphasize the difficulties in specifying representative or typical estimates of Earth location error for AVHRR satellite data.

Finally, the spatial distribution of Earth location errors for selected AVHRR satellite data has been estimated by Bordes *et al.* (1992). For most of the images they examined, the errors were more-or-less constant over the entire scene (3000–4000 scanlines). However, they found several cases where the error patterns were more complicated and varied significantly within a scene.

## 3. Correction technique

### 3.1. *Background*

#### 3.1.1. *Preliminary considerations*

AVHRR image data are initially acquired in a satellite-oriented coordinate system. Consequently, the resulting images are produced in image coordinates which are referenced to the inclined plane of the satellite's orbit and its orthogonal direction (i.e., the alongtrack and crosstrack directions). Each pixel in the image can be uniquely located by a line number for each scanline and an element number for each pixel along a given scanline. The navigation process then consists of reassigning each pixel initially given in image coordinates to an appropriate geographical location on the Earth's surface.

This transformation can be written as

Table 2. Statistics of Earth location errors for AVHRR images from three sources.

| Satellite (authors) | RMS (km) | Standard deviation (km) | Minimum error (km) | Maximum error (km) |
|---|---|---|---|---|
| NOAA-9/10 (Marsouin and Brunel 1991) | 3·2 | 0·6 | 2·0 | 4·3 |
| NOAA-11 (Bordes *et al.* 1992) | 3·3*<br>4·2 | — | — | — |
| NOAA-11 (Present work—Persian Gulf) | 5·4 | 4·1 | 1·2 | 17·9 |

*Corresponding RMS pixel (upper line) and line (lower line) errors.

$$x = \mathbf{A}(e, l)$$

$$y = \mathbf{B}(e, l)$$

where **A** and **B** represent functions which transform the image coordinates to geographical coordinates. Here, $(e, l)$ = (element, line) represents the image coordinates of a pixel, and $(x, y)$ = (longitude, latitude) represents the Earth coordinates of the same pixel in degrees of longitude and latitude. (Here, and elsewhere in the text, $y$ and $x$ refer to latitude and longitude, respectively, and differ from the alongtrack and crosstrack directions because of the inclination of the satellite's orbit).

To determine the transformation functions **A** and **B**, at least two approaches can be used, a physical model of the earth plus satellite system, or an empirical model which depends on the mathematical properties of **A** and **B**.

(*a*) The physical approach depends on the construction of orbit, attitude and sensor geometry models to generate accurate navigation (Kloster 1989, Marsouin and Brunel 1991).

(*b*) The empirical approach relies on the use of GCPs. The location of a GCP is estimated using simple, empirically-based models for **A** and **B**, where the differences between the GCP locations obtained from the satellite navigation data and an independent geographical reference are used to calculate the parameters of the model (e.g., Bernstein and Ferneyhough 1975).

Both of these approaches have limitations. Our knowledge of the precise magnitudes of the processes influencing a satellite's position in space is incomplete, and thus our models are inexact. For example, although the satellite's position in space is affected by the solar wind, ephemeris models are not able to predict this effect with great accuracy (E. Harrod, personal communication).

In using GCPs, high frequency variations in spacecraft attitude often require many well-distributed GCPs to adequately navigate an image which in turn may require the transformation functions, **A** and **B**, to be nonlinear. Moreover, the GCP approach may become computationally intensive as the number of GCPs increases.

At this point we include a brief description of the NESDIS navigation procedures. The NESDIS navigation procedures (Harrod 1990) are based on high precision orbital elements which are provided by the U.S. Navy Space Command (USNSC). These elements include an inertial position, a velocity vector with orbit numbers, a ballistic coefficient, solar flux, average solar flux, and planetary index. A numerical integrator is used to predict the velocity vector ahead for inclusion in a User Ephemeris File (UEF). The UEF contains the original USNSC velocity vector and data records at 60-second intervals for a 10-day period. The UEF is used to generate the Earth location data and the TBUS messages. The 10-day UEF is used to compute the Earth location and gridding parameters for the AVHRR data. A start time, taken from other instruments aboard the spacecraft, is used together with instrument scanning parameters and vectors from the UEF to produce the Earth location and gridding parameters. The Earth location and gridding data files are updated for a 29-hour period that starts on the following day. With respect to the orbit prediction model presently in use by NOAA/NESDIS, geographical coordinates are produced with an accuracy of approximately 0·05–0·1° (see §2). An improved ephemeris model is presently under development by NESDIS and is referred to as the Advanced Earth Location Data System (Sharma 1990).

However, for oceanographic applications, accuracies of this order are often unacceptable. In such cases, the empirical GCP approach may be used **to improve** the navigation data which are initially provided (from NESDIS or from any other source of ephemeris predictions for AVHRR satellite data).

A two-stage approach, using an orbit prediciton model to provide first-guess earth locations, followed by the use of GCPs, provides the basis for improved Earth location accuracies for regions where GCPs are available (i.e., Bordes *et al.* 1992).

This is the approach we have followed in this study.

3.1.2. *Landmarks and landmark uncertainty*

Ground Control Points (GCPs), i.e., unique geographical locations or features such as small islands, lakes, capes, etc. which are clearly visible in an image, can often be used as a basis for renavigating images where Earth location errors exist. This error is usually defined as the difference between the image location of a selected GCP and that obtained from a high resolution map or geographical database. Where a number of GCPs are taken into account, the RMS difference is often used to express the mean error.

However, the use of GCPs introduces an additional error which we refer to as landmark uncertainty. Landmark uncertainty results from our inability to accurately locate GCPs in a satellite image or map. Thus, landmark uncertainty has two sources: uncertainty in the location of a GCP in the image, and the uncertainty of its location on the corresponding map.

Uncertainty of the image coordinates is produced by the limited resolution of the human eye and the AVHRR instrument. (Objective techniques such as two-dimensional cross-correlation can be used to reduce the dependence on human judgement (e.g., Borders *et al.* 1992)). Map uncertainty depends on the scale of the map and on its cartographic accuracy. Detailed digital libraries also exist that contain high resolution coastlines plus the locations of other unique land features (Bordes *et al.* 1992, Cracknell and Paithoonwattanakij 1989). As we proceed, several terms are used to describe the spatial distributions of the GCPs:

1. The GCP region—general location of the GCPs within the image.
2. The GCP area—the actual geometric area covered by the GCPs themselves.

3.2. *The correction functions*

3.2.1. *Approach*

Let $u$ and $v$ be the approximate geographical coordinates of an image pixel. These coordinates are approximate because they are subject to small errors, thus we let

$$u = X + \varepsilon_x$$

$$v = Y + \varepsilon_y \tag{1}$$

where $X$ and $Y$ are the exact coordinates of the pixel, and $\varepsilon_x$ and $\varepsilon_y$ are the spatial components of the navigation error vector, $\varepsilon = \{\varepsilon_x, \varepsilon_y\}$, where $\varepsilon$ may also be separated into two primary frequency bands (see §2.2), i.e., high and low frequencies,

$$\varepsilon = \varepsilon^{\text{l.f.}} + \varepsilon^{\text{h.f.}}$$

or

$$\varepsilon_x = \varepsilon_x^{\text{l.f.}} + \varepsilon_x^{\text{h.f.}}$$
$$\varepsilon_y = \varepsilon_y^{\text{l.f.}} + \varepsilon_y^{\text{h.f.}} \tag{2}$$

To correct these errors, we introduce a procedure where the $u$ and $v$ coordinates assume the roles of first-guess estimates for the true values,

$$x = u + F(u, v)$$
$$y = v + G(u, v) \tag{3}$$

Here $x$ and $y$ are the corrected coordinates and $F$ and $G$ are, as yet, unspecified correction functions. We may consider the correction to be optimal when the corrected coordinates $(x, y)$ are equal to the exact coordinates $(X, Y)$. From this condition and from (1) and (3), we immediately obtain

$$F(u, v) = -\varepsilon_x$$
$$G(u, v) = -\varepsilon_y \tag{4}$$

Equation (4) defines the optimal correction functions for $F$ and $G$. To obtain solutions to (4), we introduce models for $F$ and $G$. If we knew the physical processes that cause the residual errors in navigation and their time dependence, we could construct a physical model for the correction functions, $F$ and $G$. However, as indicated earlier, our knowledge of these processes is incomplete. Therefore, we consider an empirical model based on GCPs.

Such an empirical model can be defined as

$$F(u, v) \approx f(u, v, \mathbf{a})$$
$$G(u, v) \approx g(u, v, \mathbf{b})$$

$f$ and $g$ in turn can be expanded as

$$f(u, v, \mathbf{a}) = \sum_{i=1}^{N} a_i \varphi_i(u, v)$$
$$g(u, v, \mathbf{b}) = \sum_{i=1}^{M} b_i \phi_i(u, v) \tag{5}$$

where $\mathbf{a}$ and $\mathbf{b}$ are coefficients to be determined, $\varphi(u, v)$ and $\phi(u, v)$ represent as yet unspecified basis functions, and $N$ and $M$ are the basis dimensions.

$\varphi(u, v)$ and $\phi(u, v)$ can be represented by any complete set of basis functions. If the basis functions create a complete set, we can (in principle) represent the error for a given level of accuracy by increasing $N$ and $M$ in (5) to the appropriate values. The possibility of choosing different basis functions for $\varphi(u, v)$ and $\phi(u, v)$ provides an additional degree of freedom, allowing us to fit the model to the errors more efficiently. Such flexibility allows us to improve the representation for minimal values of $N$ and $M$, which may in turn improve the convergence of (5).

Because of our lack of detailed information concerning the navigation errors mentioned previously, we use a polynomial basis as the simplest representation for expanding (5). However, we note that polynomial models with reasonably small $n$ and $m$, where $n$ and $m$ are the orders of the polynomials (not to be confused with $N$ and $M$), cannot reproduce both the high and the low frequency components of the

navigation error simultaneously. Thus, we assume that the low frequency component, $\varepsilon^{\text{l.f.}}$, is more important than $\varepsilon^{\text{h.f.}}$ (some justification for this assumption is provided in table 2). Our model can now be expressed as

$$F(u,v) \approx f_{n,m}(u,v,\mathbf{a}') = -\varepsilon_x^{\text{l.f.}}$$
$$G(u,v) \approx g_{n,m}(u,v,\mathbf{b}') = -\varepsilon_y^{\text{l.f.}} \tag{6}$$

Here $\mathbf{a}'$ and $\mathbf{b}'$ are polynomial coefficients. We note that $n$ and $m$ may be different for $f$ and $g$, providing additional flexibility in specifying the expansion, (see discussion for additional information). Because these polynomials are two-dimensional, they contain terms which are cross-products. A variety of two-dimensional polynomials can be defined which depend upon the particular terms that are retained in the expansion (Chisholm 1973). In this study, the following two-dimensional polynomials were chosen (for $n \leqslant m$),

$$f_{n,m}(x,y) = \sum_{i=1}^{n+1} \sum_{j=1}^{m+2-i} a_k x^{i-1} y^{j-1}$$

where $k = j + (m+1)(i-1) - (i-1)(i-2)/2$. The number of terms (or the number of coefficients) in this expansion is given by $N$, where

$$N = (2m - n + 2)(n+1)/2$$

Finally, substituting (6) into (3), we obtain the following equations for the corrected coordinates

$$x = u + f_{n,m}(u,v,\mathbf{a}')$$
$$y = v + g_{n,m}(u,v,\mathbf{b}') \tag{7}$$

where, according to (6), $x$ and $y$ are corrected only for the low frequency component of the error.

3.2.2. *Least-squares fitting procedures*

If $\varepsilon$ could in reality be separated into low ($\varepsilon^{\text{l.f.}}$) and high ($\varepsilon^{\text{h.f.}}$) frequency components, (6) and (7) would provide the basis for obtaining a correction for the low frequency error. The residual error in this case would be

$$\epsilon_x = X - x = \varepsilon_x^{\text{h.f.}}$$
$$\epsilon_y = Y - y = \varepsilon_y^{\text{h.f.}} \tag{8}$$

In practice, we are not able to make this separation. However, by assuming that $|\varepsilon^{\text{h.f.}}/\varepsilon^{\text{l.f.}}| \ll 1$, we consider the following alternative to (6),

$$f_{n,m}(u,v,\mathbf{a}) = -\varepsilon_x$$
$$g_{n,m}(u,v,\mathbf{b}) = -\varepsilon_y \tag{9}$$

To find solutions to (9), we apply the method of least-squares, which gives rise to the following minimization

$$\min_a \chi_f^2 = \min_a \left[ \frac{1}{K} \sum_{i=1}^{K} \frac{1}{(\omega_x^i)^2} |f_{n,m}(u_i, v_i, \mathbf{a}) - \varepsilon_x^i|^2 \right] \tag{10}$$

The condition expressed in (10) determines the minimum of a functional $\chi_f^2$ (the minimization takes place with respect to **a**) where $\omega^i$ is the landmark uncertainty for the $i$th GCP and $K$ is the number of **active** GCPs (i.e., the number of GCPs which actually take part in the least-squares fitting). Equation (10) can be written in differential form as

$$\frac{\partial \chi_f^2(a)}{\partial a_j} = 0, j = 1, 2, \ldots, N$$

which yields the following system of linear (i.e., normal) equations

$$\sum_{p=1}^{N} A_{q,p} a_p = B_q, \; q = 1, \ldots, N \tag{11}$$

The matrix $A_{q,p}$ and the vector $B_q$ can be expressed as

$$A_{p,q} = \sum_{i=1}^{K} \frac{\varphi_p(u_i, v_i)\varphi_q(u_i, v_i)}{(\omega_x^i)^2}$$

$$B_q = \sum_{i=1}^{K} \frac{(X_i - u_i)\varphi_q(u_i, v_i)}{(\omega_x^i)^2}$$

where $\varphi_q(u, v)$ and $\varphi_p(u, v)$ represent the basis functions originally introduced in (5). The solution of (11) yields the $a_i$ coefficients for the error correction function, $f$. A similar equation holds for $g$.

It is important to emphasize that **a** (i.e., the solution of (9)) differs from **a**′ (the solution of (6)) for two reasons. First the right-hand side of (6) differs from the right-hand side of (9), due to the fact that the right-hand side of (9) includes the high frequency component of the navigation error. This term acts as noise here because the polynomial expansion is incapable of reproducing both the high and the low frequency components simultaneously. Second, taking into account the landmark uncertainties $\omega_i$, which serve as weighting factors in (10), introduces additional uncertainties in the solution for **a**. This occurs in this case, because we can not distinguish between the solutions for **a**′ and $\mathbf{a} = (\mathbf{a}' + \Delta\mathbf{a})$, if both satisfy the conditon

$$|f_{n,m}(u_i, v_i, \mathbf{a}) - f_{n,m}(u_i, v_i, (\mathbf{a} + \Delta\mathbf{a}))| \leqslant \omega_i, \quad i = 1, \ldots, K$$

and that $\chi_f^2 < 1$. Further, it means that a relation between the solutions of (6) and (9) can be written

$$f_{n,m}(u, v, \mathbf{a}) = f_{n,m}(u, v, \mathbf{a}') + \delta_f(u, v) \tag{12}$$

Equation (12) shows that the correction function, $f_{n,m}(u, v, \mathbf{a})$, may be similar, but not necessarily identical, to the correction function, $f_{n,m}(u, v, \mathbf{a}')$, even when the high frequency noise is completely removed. This difference, $\delta_f(u, v)$, is small within the region covered by the GCPs, where from (10),

$$|\delta_f(u_i, v_i)| \leqslant \omega_i, \quad i = 1, \ldots, K$$

and, in general, there are no constraints on this function outside the GCP region.

For the corrected coordinates, (12) yields

$$\begin{aligned} x &= u + f_{n,m}(u, v, \mathbf{a}) = u + f_{n,m}(u, v, \mathbf{a}') + \delta_f(u, v) \\ y &= v + g_{n,m}(u\, v, \mathbf{b}) = v + g_{n,m}(u, v, \mathbf{b}') + \delta_g(u, v) \end{aligned} \tag{13}$$

where the residual errors can be expressed as

$$\epsilon_x = X - x = \delta_f(u, v) + \varepsilon_x^{\text{h.f.}}$$
$$\epsilon_y = Y - y = \delta_g(u, v) + \varepsilon_y^{\text{h.f.}} \tag{14}$$

It is evident from (14) that the residual error now has an additional component, in particular, $\delta(u, v)$, compare with (8). Within the GCP region, this contribution is limited by landmark uncertainty and the residual errors are thus constrained according to

$$\epsilon_x \leqslant \omega + \varepsilon_x^{\text{h.f.}}$$
$$\epsilon_y \leqslant \omega + \varepsilon_y^{\text{h.f.}} \tag{15}$$

where $\omega = \max(\omega_i)$. However, outside the GCP region $\delta(u, v)$ and the residual errors can be very significant (see § 3.3). In effect, $\delta(u, v)$ represents the uncertainty in extrapolation over areas far-removed from GCP regions.

### 3.3. *Extrapolation uncertainty for remote regions*

To correct errors in navigation over the ocean, our correction functions must be extrapolated. Consequently, we examine the extrapolation uncertainty within, and beyond, the GCP region. The extrapolation uncertainty ($\delta$) has four primary sources:

1. *Landmark uncertainty*. The greater the landmark uncertainty, the less the sensitivity of the least-squares method to variations in the coefficients **a** and **b**, and the greater $\Delta\mathbf{a}$ and $\Delta\mathbf{b}$ will be. Also, $\delta(u, v)$ will be greater outside the GCP region and the resulting extrapolations will be less stable.
2. *Distribution of landmarks*. Both the relative size of the GCP region and the spatial distribution of GCPs strongly affect extrapolation accuracy and stability. The greater the area covered by the GCPs and the more uniform their distribution, the greater the accuracy and stability of the extrapolation.
3. *The number of GCPs*. In general, the greater the number of the independent GCPs (see § 3.3.3), the higher the accuracy of the extrapolation.
4. *The high frequency component of the navigation error*. The greater the high frequency error component, $\varepsilon^{\text{h.f.}}$, the greater $\delta(u, v)$ will be outside the GCP region, with a corresponding decrease in the accuracy and stability of the extrapolation (see § 3.2. and 4.1 for details).

#### 3.3.1. *Estimation of extrapolation uncertainty*

We are not able to estimate $\varepsilon^{\text{h.f.}}$ in areas far-removed from landmarks, but we can estimate $\delta(u, v)$, using (5) if we know $\Delta\mathbf{a}$ (or $\Delta\mathbf{b}$), since

$$\delta_f^2(u, v) = \sum_{i=1}^{N} \left| \frac{\partial f(u, v, \mathbf{a})}{\partial a_i} \right|^2 \Delta a_i^2 = \sum_{i=1}^{N} |\varphi_i(u, v)|^2 \Delta a_i^2 \tag{16}$$

To estimate $\Delta\mathbf{a}$ (or $\Delta\mathbf{b}$) we calculate the covariance matrix **D** which is the inverse of the Hessian matrix, **H** (a matrix whose components are second-order partial derivatives), where

$$\mathbf{D} = \mathbf{H}^{-1}$$

and where **H** can be expressed as

$$\mathbf{H}_{i,j}=\frac{1}{2}\frac{\partial^2\chi^2}{\partial a_i \partial a_j} \tag{17}$$

From (10) we obtain the following relationship for **H**,

$$\mathbf{H}_{i,j}=\sum_{l=1}^{K}\frac{\varphi_i(u_l, v_l)\varphi_j(u_l, v_l)}{\omega_l^2} \tag{18}$$

Now, $\Delta\mathbf{a}$ can be found from the diagonal elements of **D**, where

$$\Delta a_i=\sqrt{\mathbf{D}_{i,i}} \tag{19}$$

By substituting $\Delta a_i$ in (16), we obtain an estimate for the error associated with the extrapolation of the navigation error correction function. Expressions (16)–(19) are thus useful in estimating the extrapolation uncertainty in areas far-removed from landmarks.

3.3.2. *Landmark distributions*

From the above, it follows that greater accuracy in the interpolation of the correction functions inside GCP regions does not necessarily correspond to greater accuracy in the extrapolation of the correction functions beyond the GCP regions. To evaluate the accuracy of our correction procedures outside the GCP region, additional GCPs or **spectator** locations can be introduced. These so-called spectators do not take part in the least-squares fitting and thus can be used independently to check the accuracy of our extrapolation (or interpolation) procedures.

The accuracy of our correction procedures depends strongly on the location, distribution and number of **active** GCPs. If active GCPs cover only a small portion of the scene (a situation often encountered in oceanographic applications), we expect lower extrapolation accuracy over the ocean. To distinguish between different GCP configurations, we introduce a new coefficient which we refer to as a 'spanning' coefficient. It indicates the approximate ratio of the effective area covered by the GCPs, to the area covered by the image.

With respect to this spanning coefficient, we first define a 'centre of mass' and an effective size for the active GCP region. The coordinates $(x_c, y_c)$ represent the centre of mass of the GCP region if the following mean values are taken

$$x_c=\frac{1}{K}\sum_{i=1}^{K}x_i$$

$$y_c=\frac{1}{K}\sum_{i=1}^{K}y_i \tag{20}$$

where $K$ represents the number of active GCPs. Next, the rectilinear distance of any point in the image $(x_i, y_i)$ from the centre of mass of the GCP region can be expressed as

$$r_i=\sqrt{(x_i-x_c)^2+(y_i-y_c)^2} \tag{21}$$

We can also define an effective size R of the GCP region as

$$R=\frac{1}{K}\sum_{i=1}^{K}r_i \tag{22}$$

and the corresponding effective area, $s$, as

$$s=\pi R^2 \tag{23}$$

Thus, with respect to the original GCP region, we have now introduced a circle of radius $R$ whose centre is located at the point $(x_c, y_c)$. The area of the circle defines an effective GCP area which, in general, differs from the geometric area of the region covered by the GCPs. For our purposes, this parameter is useful in describing particular GCP configurations.

We now define the above-mentioned spanning coefficient as

$$\alpha=s/S \tag{24}$$

where $S$ is the area covered by the image. Thus $\alpha$ represents that portion of the image which is effectively covered by the GCPs. That is, $\alpha$ per cent of the image pixels are located inside the effective GCP region, and thus $(1-\alpha)$ per cent are located outside this region. In the following section we show that the spanning coefficient, $\alpha$, allows us to distinguish between different GCP configurations as well as to estimate *in advance* the accuracy of the correction.

3.3.3. *The number of landmarks and their independence*

The minimum number of GCPs which is required to extract the coefficients of the model functions $f$ and $g$ is determined by

$$n_{\text{d.f.}} \geqslant 0 \tag{25}$$

where $n_{\text{d.f.}}$ represents the number of degrees-of-freedom which in this case can be defined as

$$n_{\text{d.f.}} = K - N \tag{26}$$

where $K$ is the number of active GCPs and $N$ is the number of unknown coefficients contained in (11).

From (25) and (26), we obtain the following important requirements, first that $K \geqslant 3$ for first-order polynomial expansions, and second, that $K \geqslant 6$ for second-order expansions. Thus, these values of $K$ provide lower limits for the number of GCPs that are required when using first- and second-order polynomials.

Finally, two GCPs are independent if

$$d_{ij} > (\omega_i + \omega_j) \tag{27}$$

where $d_{ij}$ is the distance between the $i$th and $j$th GCPs and $\omega_i$ and $\omega_j$ represent the uncertainties associated with the $i$th and $j$th GCPs. If two GCPs do not satisfy the condition expressed in (27), they are not independent; thus at least one of them could be excluded from the set of active GCPs which are initially chosen.

## 4. Verification of the method

In this section we apply our method of correcting AVHRR Earth location data first to simulated satellite data and then to several AVHRR images. Our goals are to verify the method, to estimate its accuracy, and to determine to what extent it is stable (i.e., when accuracy increases monotonically with increasing order of the polynomial expansion). We also wish to find acceptable values for the degree of the correction polynomials, the spanning coefficient, and the number of GCPs and their configurations.

4.1. *Simulated images*

4.1.1. *Simulations*

To investigate the behaviour of our renavigation procedures systematically, we simulate images with different land/ocean configurations and with different distributions of GCPs, including independent GCPs (spectators) located over remote (i.e., oceanic) regions.

The following function was chosen to simulate the low frequency error

$$\varepsilon_{sim}^{\text{l.f.}} = \exp(-u+v) \tag{28}$$

where $u$ and $v$ represent the pixel locations in image coordinates. The function expressed in (28) is nonperiodic and nonpolynomial; it varies slowly over the image and, therefore, is representative of a broad class of low frequency errors. Because we have little information about the high frequency component of the navigation error, Gaussian random noise was used to simulate the high frequency errors (Press *et al.* 1990). The dimensions of the simulated images were 11 by 11. The total simulated error according to (9) is then

$$\varepsilon_{sim} = \varepsilon_{sim}^{\text{l.f.}} + \varepsilon_{sim}^{\text{h.f.}} \tag{29}$$

with a noise-to-signal ratio ($\beta$) given by

$$\beta = \varepsilon_{sim}^{\text{h.f.}} / \varepsilon_{sim}^{\text{l.f.}} \tag{30}$$

Each simulated image has been separated into two geographical regions, 'land' and 'ocean' (figure 4). Twenty-five active GCPs were chosen over land in each case. The simulated error from (29) at these points has been used in (9), (10) and (11) to determine the correction functions, $f$ and $g$. Next, $f$ and $g$ were used to calculate a navigation correction for spectator locations over the oceanic regions. All the pixels in this region were used as spectators (not shown in figure 4). These spectator locations are not used in the least-squares fitting; we use them only to check the accuracy of our method. For each spectator location we calculate an extrapolation error, $e$, where we define this error as

$$e = |\varepsilon_{sim} - f_{n,m}| / \varepsilon_{sim}$$

and a mean extrapolation error over the oceanic region, as

$$E = \text{Mean } \{e\} \text{ 100 per cent}$$

4.1.2. *The accuracy and stability of the extrapolation procedure*

The four simulated images shown in figure 4 represent four different situations: land on one, two, three and four sides of the image. For each image, 25 active GCPs are uniformly distributed over land, and the land occupies approximately one half of the total area. We use the parameter $\alpha$ which was introduced in (24) to distinguish between the different GCP configurations; in the cases shown, it varies between 0·41 (*a*) and 0·95 (*d*).

Figure 5 shows the accuracy of the extrapolation of the correction functions over the ocean versus $\beta$ (i.e., the noise-to-signal ratio) for different orders of polynomials for the GCP configurations shown in figure 4. The accuracy and stability (with respect to the order of the polynomial and the noise level) of the extrapolation depend strongly on $\alpha$ and $\beta$. As $\alpha$ increases, the extrapolation accuracy increases; as $\beta$ increases, the extrapolation accuracy decreases.

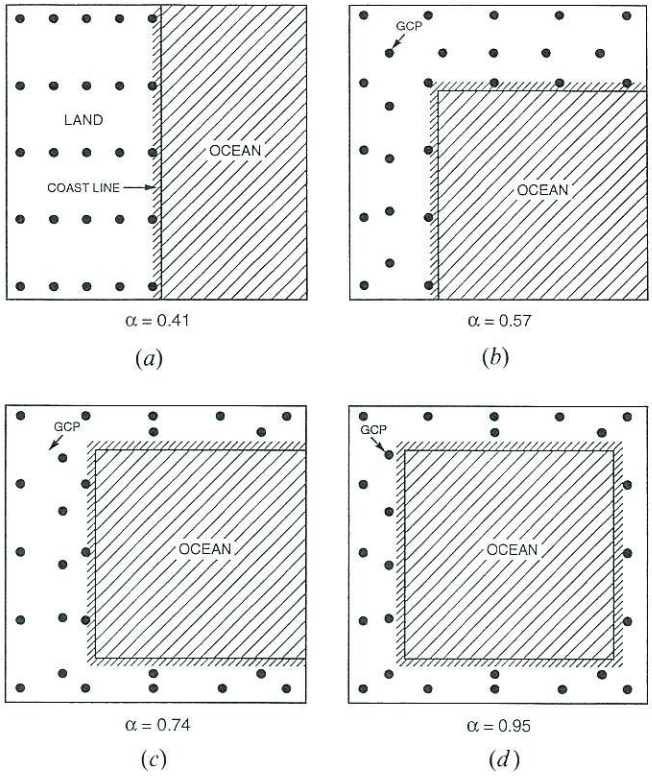


Figure 4. Four different 'land'+'ocean' configurations. The black dots represent GCPs. Corresponding values of $\alpha$ are shown in each case (see § 3.2.3).

For the most favourable configuration (land on four sides—figures 4(*d*) and 5(*d*)), the correction procedure is acceptable (of the order of the noise) for polynomial orders from 1 to 4 over a wide range of $\beta$'s. For these orders of polynomials and for $\beta \leqslant 0{\cdot}2$, the correction is stable.

A contrasting situation is illustrated in figures 4(*a*) and 5(*a*) with land on one side only. In this case, the polynomials of first- and second-order produce acceptable extrapolations, while a fourth-order polynomial is unstable, even for small $\beta$. Figures 4(*b*) and (*c*) and 5(*b*) and (*c*) represent intermediate situations.

These examples demonstrate that polynomials of order three or higher usually yield unstable extrapolations and thus can only be used under extremely favourable conditions (for very low noise levels, with $\alpha > 0{\cdot}75$). Since these conditions are usually quite unrealistic, we exclude polynomials of order three or higher from further consideration. We have also omitted zero-order corrections to simplify the figures.

Next, approximately 100 simulations were generated for different configurations again using 25 GCPs with $\alpha$'s ranging from 0·25 to 1·0 for first- and second-order polynomials. Two slightly overlapping envelopes for correction accuracy over the ocean are plotted versus $\alpha$ (figure 6(*a*)). The noise-to-signal ratio was 0·1 in all cases.

The second-order polynomial provides a better correction than the first-order polynomial only for $\alpha > 0{\cdot}5$. Thus, to benefit from a second-order correction, $\alpha$'s in this range or higher will be required (especially for higher noise levels—see figure 5).

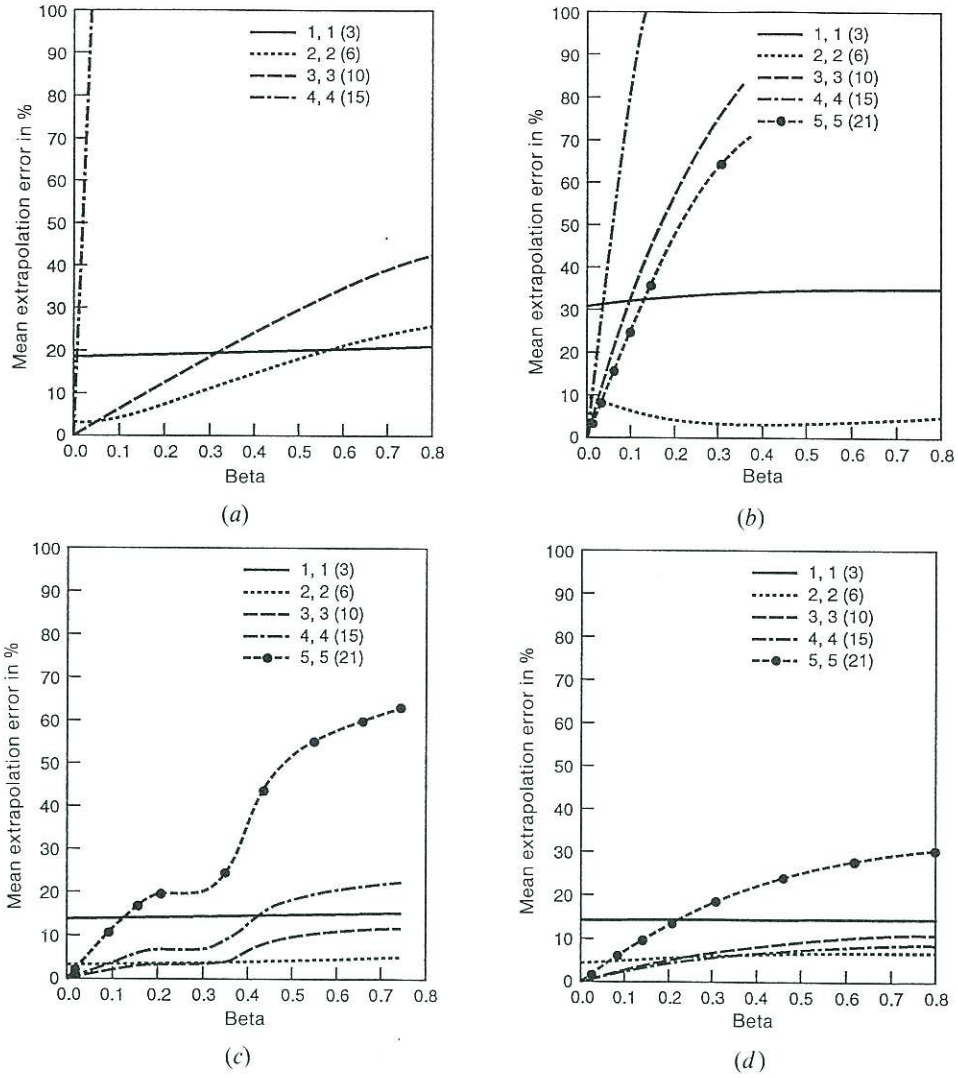


Figure 5. Extrapolation accuracy versus noise-to-signal ratio (Beta) for the four configurations shown in figure 4, for different orders of the correction polynomials. The notation '$n, m(1)$' indicates the order of the polynomials in the $x(n)$ and $y(m)$ directions respectively, and '(1)', the number of polynomial coefficients used in the least squares fitting.

Next, we investigate the dependence of extrapolation accuracy on the number of active GCPs. We started with the configuration shown in figure 4(*c*) ($\alpha \approx 0{\cdot}74$) and then varied the number of GCPs from 3 to 25, keeping their distributions uniform. A noise-to-signal ratio of 0·1 was used throughout. Figure 6(*b*) shows two envelopes for correction accuracy over the ocean for polynomials of first- and second-order. For the cases shown, the extrapolation accuracy is acceptable even for the minimum number of GCPs (i.e., three for first-order and six for second-order—note that these results are in agreement with our previous results from §3.3.3) if the noise level is

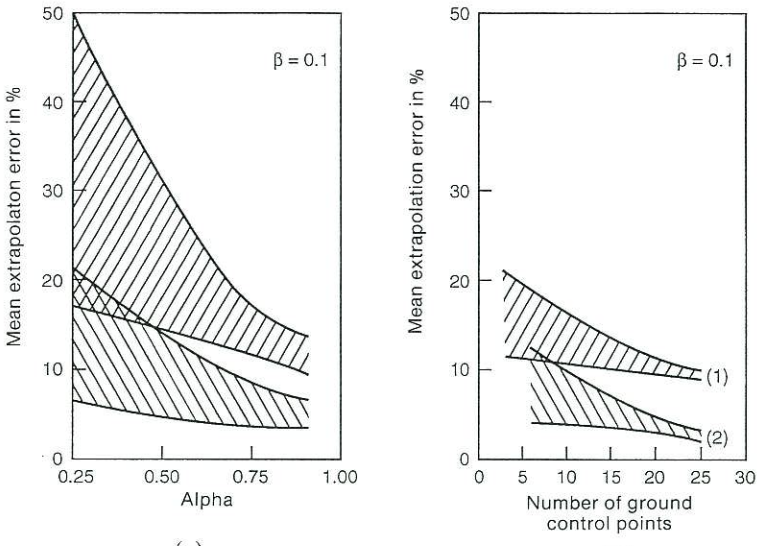


Figure 6. (*a*) Correction accuracy over the 'ocean' versus the interpolation coefficient, $\alpha$. The upper envelope represents a first-order correction and the lower envelope, a second-order correction. The noise-to-signal ratio ($\beta$) is 0·1. (*b*) Correction accuracy over the 'ocean' versus the number of the active GCPs. The upper envelope represents a first-order correction (1) and the lower envelope, a second-order correction (2). The noise-to-signal ratio is 0·1. For a first-order polynomial, the cutoff occurs for $K=3$, and for second-order, for $K=6$ (see § 3.3.3).

sufficiently low ($\beta<0{\cdot}2$), and for acceptable GCP configurations ($\alpha>0{\cdot}6$). Additional calculations were performed for $\beta=0{\cdot}2$, 0·3 and for $0{\cdot}6<\alpha<0{\cdot}74$; although these calculations are not shown, they were helpful in providing a more complete basis for interpreting these results.

Finally, figure 7 shows a three-dimensional layout for two different sets of corrections, panels (*a*)–(*d*) and (*e*)–(*h*). The original simulated errors are the same in both cases (see panels (*a*) and (*e*)). The number of active GCPs is also the same in each case ($K=7$). The only difference between these corrections is the GCP configurations that were used. For the first set of images (*a*–*d*), $\alpha\approx0{\cdot}45$, and for the second set (*e*–*h*), $\alpha\approx0{\cdot}2$. The first set shows acceptable corrections. The second set corresponds to a situation where only the coastline or a narrow coastal strip was available for locating GCPs. For the second set, the error is not adequately corrected over most of the image except for the small region occupied by the GCPs themselves. Increasing the order of the polynomial does not help in this case. However, increasing the order of the polynomial does improve the correction over the immediate GCP region. If only seven active GCPs had been available and we had calculated the corrections only at these points, we would have been unaware of the significant navigational errors that occurred over the ocean. This example emphasizes the importance of GCP distributions and the use of spectators for assessing the results of such least squares fitting procedures.

4.2. *AVHRR images*

We have also applied our navigational correction procedures to actual AVHRR images for two different areas, the Persian Gulf (PG) and the Gulf of Mexico (GM).

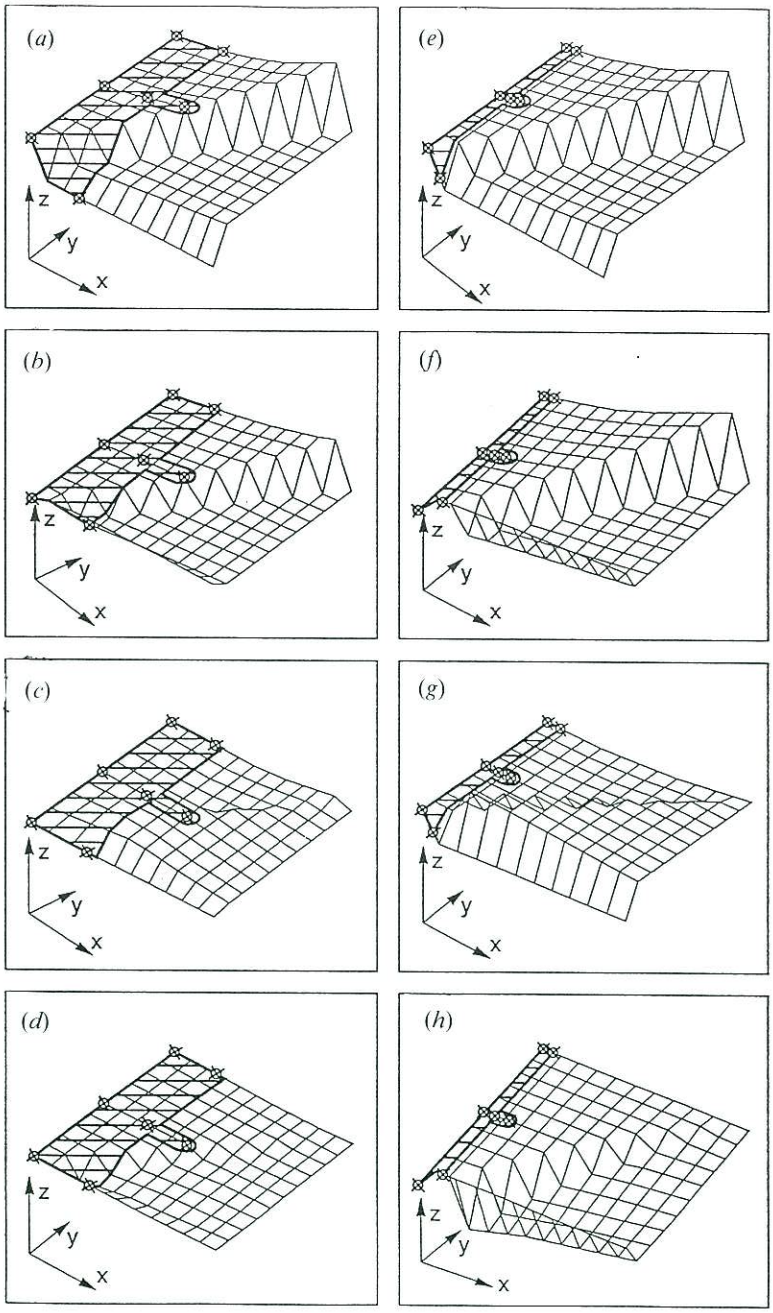


Figure 7. Three-dimensional layout for cases of acceptable (*a–d*) and unacceptable (*e–h*) corrections. The *x* and *y* axes correspond to longitude and latitude respectively. Panels (*a*) and (*e*) show initial errors before corrections for two different GCP configurations (*z* axis represents the initial error). For panels (*b*) and (*f*), the *z* axis represents the residual error after a zero-order correction, panels (*c*) and (*g*), the results after a first-order correction, and panels (*d*) and (*h*), the results after a second-order correction.

Fifteen GCPs were used for the PG image and 22 for the GM image. Certain GCPs were active sites, while other GCPs were used as spectators. Earlier (§ 2.3) we indicated that the navigation errors for these two images were significantly different, with an RMS error of 3·6 km for the PG image and an RMS error of 15·5 km for the GM image. Also, the spatial variations of the errors for the two images were very different (see figures 8 and 11). Without more specific information, we have taken the standard deviations of these errors as estimates for the high frequency error. Our estimates of noise-to-signal ratio for these images were $\beta \approx 0{\cdot}5$ for PG and $\beta \approx 0{\cdot}25$ for GM. ($\beta$ was estimated by simply taking the ratio of the standard deviation of the error to the total RMS error).

4.2.1. *The GM image*

For the Gulf of Mexico image, 22 GCPs were employed and their coordinates were obtained both from the image (NESDIS navigated, resolution of 4·4 km) and from a high-resolution map (NOS Chart Number 411, Scale of 1:2 160 000). For each GCP, several estimates of location were obtained. The mean values of the corresponding latitudes and longitudes were then used as the final coordinates of the

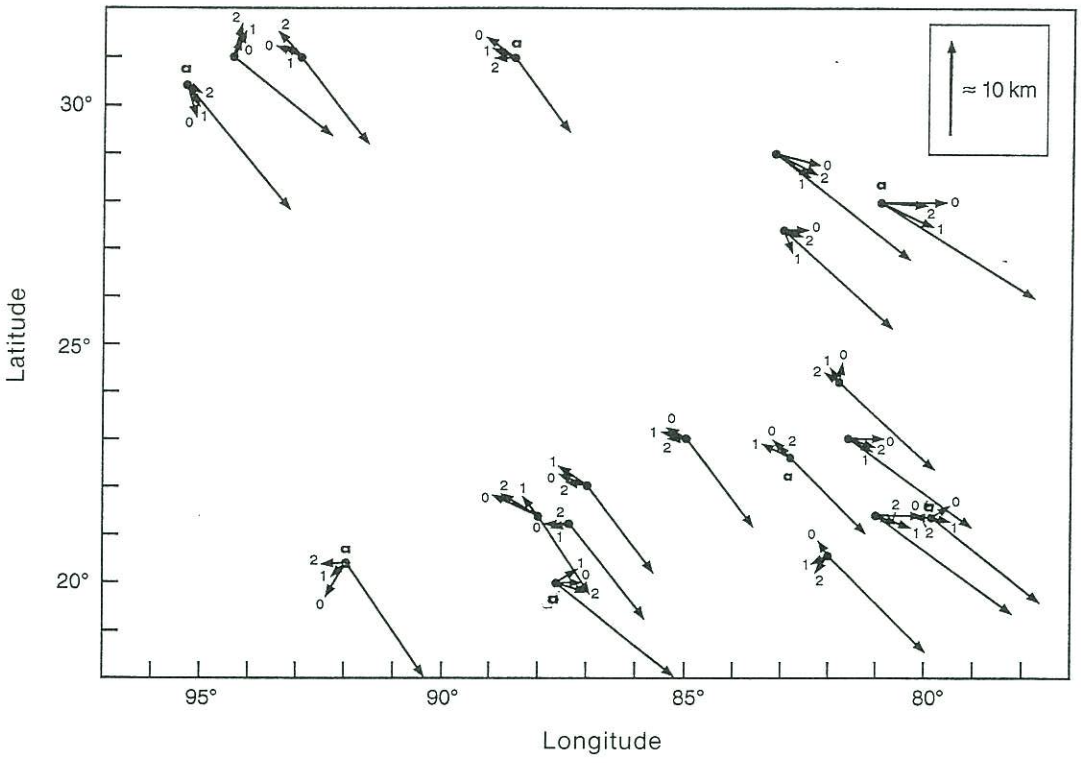


Figure 8. Spatial distribution of initial errors in Earth location and the corresponding corrections in Earth location for 19 locations around the Gulf of Mexico. The arrows without numbers represent the initial errors; the arrows with 'zeroes' represent the residual errors after zero-order corrections were applied; 'ones' indicate the residual errors after first-order corrections, and 'twos', after second-order corrections. Only seven active GCPs (identified by 'a's') were used in this renavigation procedure.

GCP and the standard deviations taken as a measure of landmark uncertainty. For the corrected field shown in figure 8, seven uniformly distributed GCPs were chosen to take part in the least-squares fitting (active GCPs), with the other 15 GCPs serving as spectators to evaluate the quality of the correction.

Table 3 shows the RMS error before and after the correction using different orders of polynomials (from 0 to 2). Because the original errors in this case varied slowly in space (and all of the original error vectors have approximately the same direction—figure 8), a simple zero-order correction provides excellent results. A first-order correction reduces the RMS error even further. However, a second-order correction gives no improvement. This result is consistent with the relatively small values of $\alpha$ ($\alpha \approx 0{\cdot}5$) in this case. As in the previous simulations, we would have been unaware of the true situation when applying a second-order correction without the use of spectators.

According to figure 6(*b*) and table 3, increasing the number of active GCPs improves the accuracy of the correction in this case and further improvement occurs when a second-order correction is applied.

In order to interpret the figures that follow, we introduce the following ideas and notation. In correcting AVHRR navigation data, we effectively shift each pixel in accordance with the value obtained from the correction function at a particular location. The actual shifts in $x$ and $y$ can be calculated as

$$n_x = f(u, v, \mathbf{a})/\theta$$
$$n_y = g(u, v, \mathbf{b})/\theta \tag{31}$$

where $\theta$ is the resolution of the image, $f$ and $g$ are the longitude and latitude correction functions, and $n_x$ and $n_y$ are the shifts (in pixels). We now introduce the parameter, $\mu$, where

$$\mu = \mathrm{INT}((n_x^2 + n_y^2)^{1/2}) \tag{32}$$

which yields an integer value (here 'INT' indicates taking the integer result (as in FORTRAN)) or shift in pixels for the effective correction for each location in the image.

Figure 9 shows $|n_x|$, $|n_y|$, and $\mu$ for first-order (*a–c*) and second-order (*d–f*) corrections. The second-order correction produces similar but more complicated nonlinear patterns, responding more closely to errors with complicated spatial structure. We note that only the magnitudes of the correction field have been

Table 3. Correction accuracy for GM image for different polynomial orders.

| | 7 Active GCPs | | 12 Active GCPs | |
|---|---|---|---|---|
| Order of polynomial | RMS error for 7 active GCPs (km) | RMS error for 15 spectators (km) | RMS error for 12 active GCPs (km) | RMS error for 10 spectators (km) |
| Before correction | 15·7 | 15·5 | 15·4 | 14·8 |
| 0 | 4·5 | 4·7 | 4·4 | 4·6 |
| 1 | 4·2 | 4·4 | 2·8 | 3·9 |
| 2 | 3·5 | 4·6 | 2·3 | 3·5 |

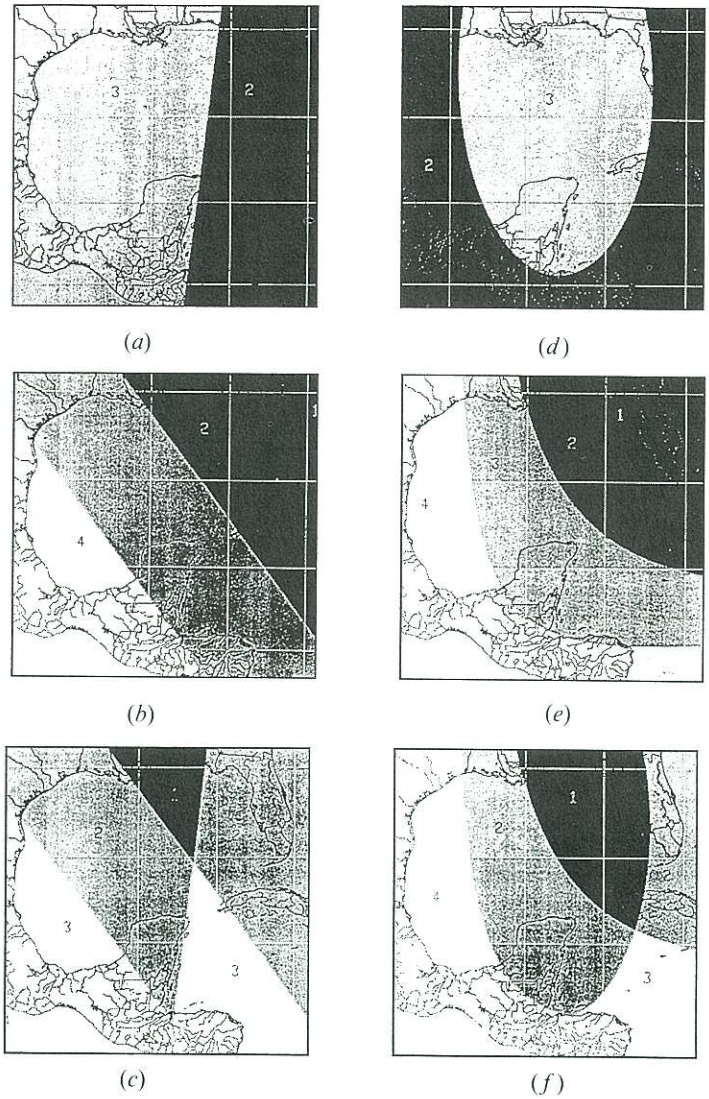


Figure 9. Correction displacement (integer values indicate the shifts in numbers of pixels) for the Gulf of Mexico image for first-order (*a–c*) and second-order (*d–f*) corrections. Panels *a* and *d* indicate shifts in the *x* direction, panels *b* and *e* indicate the shifts in the *y* direction, and panels *c* and *f* indicate the overall (vector) shifts, $\mu$. Resolution of the image is 4·4 km.

displayed in figure 9 (and in figure 12) and that to show the entire correction field, a corresponding figure showing the phase or direction of the correction would also be required.

Next, we have taken seven active GCPs (the remaining 15 GCPs were used as spectators) and examined the accuracy and stability of the extrapolation with respect to three GCP configurations (figure 10). For all three configurations, $\alpha \leqslant 0{\cdot}55$. In the first configuration, (*a*), there is land on two sides of the image. In the second

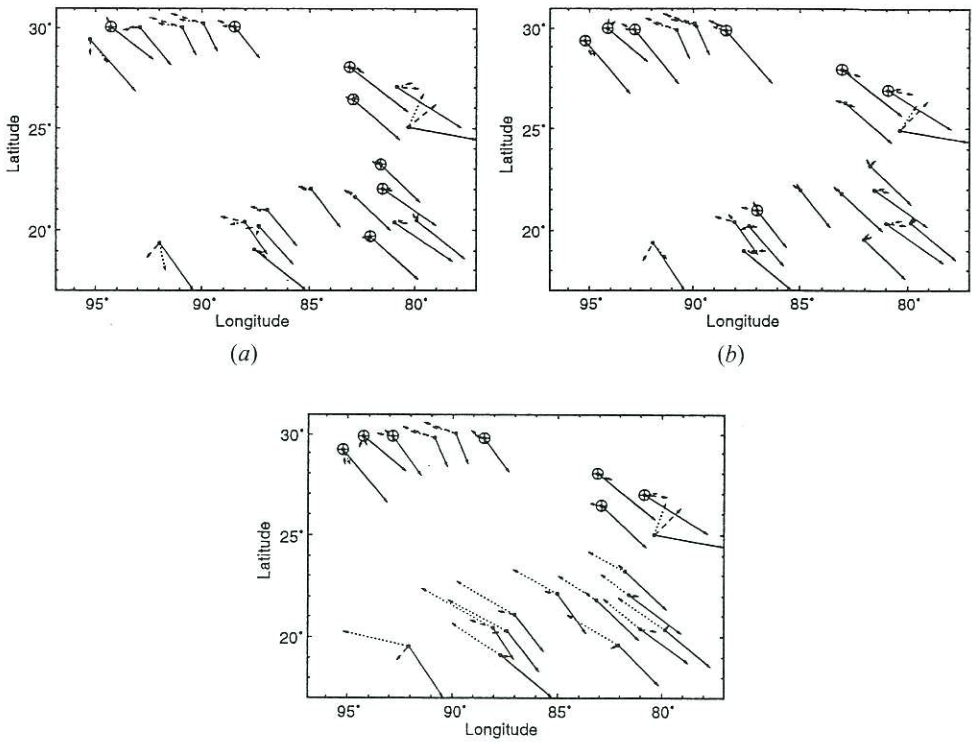


Figure 10. Zero- and first-order corrections for the Gulf of Mexico image. Three different GCP configurations are represented in (*a*), (*b*) and (*c*). The active GCPs are indicated by crossed circles. There are seven in each case but their locations vary, as indicated. Solid arrows represent the initial errors, the dashed arrows represent the residual errors after a zero-order correction and the dotted arrows represent the residual errors after a first-order correction.

configuration, (*b*), there is land on one side of the image with a remote island located over the ocean, and in the third configuration, (*c*), there is land on one side of the image with the GCPs concentrated near the coastline.

Table 4 shows the accuracy of the corrections for the three GCP configurations shown in figure 10. Because the $\alpha$'s are less than about 0·5 in each case, we do not expect improved results using a second-order correction. The results shown in table 4 indicate that configuration (*c*) provides the poorest results in areas far-removed from the GCPs. Only the zero-order correction provides acceptable results for this configuration. Configurations (*a*) and (*b*) include a first-order correction and show improvement over the zero-order correction in these cases.

As before, without spectators, all configurations would have produced results which were apparently similar, and second-order corrections would most likely have been chosen in each case. These results are due to the least-squares method which is used to calculate the coefficients of the terms in the polynomial expansions. In each case, the higher the order of the polynomial employed, the better the fit to the active GCP locations. Since the spectators are not used in the least-squares fitting, the

Table 4. Correction accuracy for the different GCP configurations shown in figure 10.

| Configuration | (*a*) | | (*b*) | | (*c*) | |
|---|---|---|---|---|---|---|
| Order of polynomial | RMS error for 7 active GCPs (km) | RMS error for 15 spectators (km) | RMS error for 7 active GCPs (km) | RMS error for 15 spectators (km) | RMS error for 7 active GCPs (km) | RMS error for 15 spectators (km) |
| Before correction | 16·1 | 15·8 | 16·3 | 15·6 | 16·8 | 15·5 |
| 0 | 2·8 | 4·9 | 4·5 | 4·7 | 4·1 | 4·8 |
| 1 | 2·5 | 4·6 | 3·6 | 4·4 | 3·2 | 12·0 |
| 2 | 1·2 | 5·2 | 1·3 | 25·1 | 1·5 | 89·4 |

Table 5. Correction accuracy for PG image for different polynomial orders.

| | 4 Active GCPs | | 7 Active GCPs | |
|---|---|---|---|---|
| Order of polynomial | RMS error for 4 active GCPs (km) | RMS error for 11 spectators (km) | RMS error for 7 active GCPs (km) | RMS error for 8 spectators (km) |
| Before correction | 3·7 | 3·5 | 3·4 | 3·8 |
| 0 | 2·8 | 2·7 | 2·5 | 2·4 |
| 1 | 1·3 | 1·7 | 1·2 | 1·3 |
| 2 | N/A | N/A | 1·1 | 1·6 |

errors for spectators become very sensitive to extrapolation uncertainty, particularly when they are located outside the GCP region.

4.2.2. *The PG image*

In the Persian Gulf image (NESDIS navigated, resolution 2·2 km), 15 GCPs were used and their coordinates and uncertainties obtained as before. First four, and then seven, (only corrections using seven active GCPs are shown in figure 11) uniformly distributed active GCPs were used in the least-squares fitting. The remaining GCPs were used as spectators in each case.

Table 5 shows the RMS errors before and after correction, using polynomials of order 0 to 2. The initial errors were variable in space (figure 11); however, only a first-order correction was required to reduce the errors significantly, and a second-order correction provided no further improvement. Alpha ($\alpha$) was about 0·6 in this case; hence, we might have expected better results by applying a second-order correction. However, the noise-to-signal ratio was $>0{\cdot}5$ and consequently reduced the accuracy of the second-order correction because of greater extrapolation uncertainty.

Panels (*a*) and (*b*) in figure 12 show the first- and second-order corrections obtained from equation (32). The first-order correction field (magnitude only) is

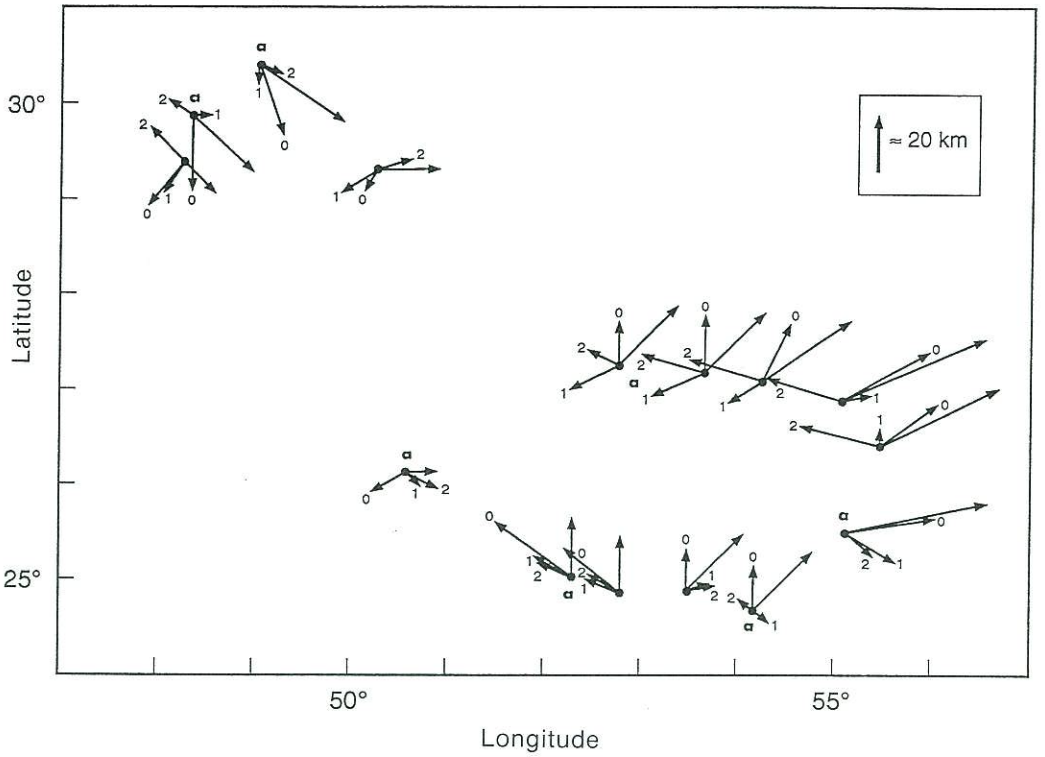


Figure 11. The same as figure 8 but for 15 landmarks around the Persian Gulf. Only seven active GCPs (identified by 'a's') were used in this renavigation procedure.

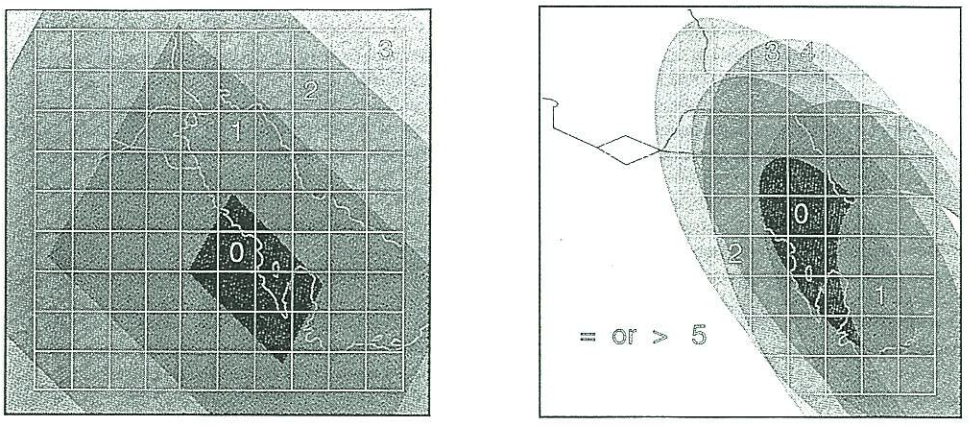


(*a*) (*b*)

Figure 12. Navigation corrections (integer values indicate the shifts in pixels) for Persian Gulf image for first-order (*a*) and second-order (*b*) corrections. Resolution of the image is 2·2 km.

box-like and linear, but the second-order correction is nonlinear and increases rapidly outside the GCP region because the extrapolation uncertainty is high.

## 5. Discussion

The navigation correction procedures presented in this study are based on the use of GCPs. All of the required information is introduced through the GCPs, including the navigation errors, landmark uncertainties, GCP configurations and the high frequency noise. Thus, the correction accuracy depends strongly on the particular selection of GCPs.

Recommendations on how to (1) choose the number of active GCPs, (2) improve the configuration of the active GCPs which are selected, and (3), choose the order of the correction polynomials, were made. The concept of noise-to-signal ratio was introduced and its impact on the quality of the renavigation process illustrated. There are significant uncertainties associated with estimating the noise-to-signal ratio. We have proposed only one very approximate method for estimating this parameter. Hence, there is ample room for improvement in this area.

We now consider several possibilities for improving the noise-to-signal ratio and thus the quality of the renavigated data. With respect to the noise-to-signal ratio, one of the most serious problems encountered during this study was the occurrence of high frequency errors in the AVHRR navigation data. These errors have spatial scales which are of the order of, or less than, the dimensions of a typical scene, i.e., about 2000 km. We assume that these errors are primarily due to rapid variations in spacecraft attitude although other unknown factors may also contribute. How often such high frequency errors occur in AVHRR navigation data is not known but their occurrence, even if infrequent, raises the possibility that when they occur, they may go undetected. Clearly, the best solution to this problem would be to assimilate information on spacecraft attitude directly into ephemeris model calculations.

Other possibilities also exist for improving the noise-to-signal ratio. For images where high frequency errors occur, only a few, or perhaps no GCPs will be located in the areas where the navigation errors are greatest. However, the effect of including GCPs from such areas will be to degrade the accuracy of the corrections elsewhere in the image. Excluding such 'noisy' GCPs from the complete set of active GCPs will improve the noise-to-signal ratio and, therefore, the accuracy of the corrections.

One method of identifying noisy GCPs is based on the fact that the Earth location errors for GCPs located in areas which contain high frequency distortion differ significantly from the errors of their neighbours. Thus, we may initially remove noisy GCPs so identified from the set of active GCPs before we apply the correction procedures.

However, for regions where several GCPs are included in areas of high local distortion, simple 'preselection' procedures may not be easy to apply. In these cases, a more sophisticated, 'postselection' approach may be applied. This approach relies on the fact that low-order polynomials are stable with respect to high frequency noise. Thus, low-order polynomials do not fit noisy GCPs as well as they fit noise-free GCPs. After the corrections are calculated, noisy GCPs can be recognized as those with deviations which are significantly greater than the deviations of their neighbours. The extrapolation uncertainty can then be used to recognize noisy or redundant GCPs as those that maximize the extrapolation uncertainty as estimated from equation (16).

Considerable attention was given to determining the optimal order of the polynomials that are used to generate the navigation corrections. The correction functions were initially presented as separate functions of $x$ and $y$ in equation (3). This separation was not only convenient mathematically, but has a physical basis as well since the sources of navigation error such as roll, pitch and timing are aligned in either the alongtrack or the alongscan directions. Consequently it may be possible to improve the polynomial order selection by considering different orders for each direction. Furthermore, it may be possible to use different bases for $x$ and $y$ to optimize the fit of the mathematical model to the physical characteristics of the errors. Finally, since polynomial correction functions are two-dimensional, various cross-product terms arise in their expansions. Thus, even further flexibility arises through the choice of terms which ultimately provide the best renavigation accuracies. Although we have not explored these various possibilities, they merit further consideration.

## 6. Summary and recommendations

General correction procedures for improving navigation accuracy for AVHRR satellite data using GCPs were presented. Although earlier studies provided a basis for the present study, a number of new topics and techniques have been introduced. Particular emphasis has been put on the extrapolation of navigation corrections over oceanic regions far-removed from ground control (i.e., landmarks). Sources of landmark uncertainty were identified and the dependence of renavigation accuracy on landmark uncertainty and the distribution of GCPs was investigated. Correction functions were derived as expansions for any complete basis. A single parameter, $\alpha$, was introduced to quantitatively describe the configurations of GCPs. Acceptable values for this parameter and the minimal number of GCPs for various conditions were proposed. Criteria for establishing the independence of GCPs and for calculating the minimum number of GCPs were introduced. A least-squares procedure was used which took into account landmark uncertainty. A particular basis using polynomial expansions was presented and optimal orders for these polynomials were obtained.

The problem of local (high frequency) variations in navigation error and its relationship to the quality of the corrections was examined. The problem of extrapolating navigation corrections over remote regions was examined and quantified. Finally, new procedures for evaluating the quality of renavigated data were applied to both simulated and actual AVHRR images including the use of independent, i.e., spectator, locations for determining the overall accuracy of the corrections.

A technique for estimating extrapolation uncertainty was also presented. Pre- and postselection procedures for selecting GCPs were proposed to reduce the influence of local navigation errors.

It is recommended that the geometric area covered by GCPs should be as large as possible. The distribution of GCPs inside the GCP region should be uniform; the GCPs should also be independent, where possible. Along the U.S. west coast, for example, land is often available on only one side of a typical scene, a situation which limits the opportunities for good ground control. In these cases it is recommended that satellite coverage be acquired as far inland as possible to obtain more, and better-distributed, GCPs for renavigation.

Polynomials of order higher than two should not be used to navigation except under extremely favourable conditions, and ev polynomials should not be used in all cases. Under unfavourable the noise-to-signal ratio is relatively high ($\beta > 0{\cdot}5$) and/or the GCP poor ($\alpha < 0{\cdot}4$), only polynomials of zero-order may give acceptable

Also, we emphasize that the rules and recommendations presented for evaluating navigational errors should not be interpr rather that they should serve as starting points for additional work this area.

Finally, because high-frequency errors in satellite navigation ma in areas where no GCPs exist, it is strongly recommended that spacecraft attitude including roll, pitch and yaw be assimilate operational ephemeris models during the process of calculating ea the AVHRR satellite data.

Although this study focussed primarily on correcting navigatio AVHRR, the techniques presented here should apply equally we sensors on other spacecraft as well, including both polar-orbiting nous satellites.

**Acknowledgments**

This study was completed with support from NOAA's COAS gram, (a project of NOAA's Coastal Ocean Program). The authors w following individuals for help and encouragement during the cour Walt Campbell, Joann Nault, Emily Harrod, Irwin Ruff, Lou Barb Bill Tseng, D. B. Rao, Mark Waters and Michael Pecnick. We pa Lee Ranne for providing the data on spacecraft attitude shown i Geary for producing figures 9 and 12, David Solomon for provid information contained in table 1 and Jim Shepherd for providing yaw measurement. We would also like to thank one of the reviewers very detailed and thoughtful comments.

**References**

BERNSTEIN, R., and FERNEYHOUGH, JR., D. G., 1975, Digital image proces *metric Engineering and Remote Sensing*, **41,** 1465–1476.

BORDES, P., BRUNEL, P., and MARSOUIN, A., 1992, Automatic Adjustm Navigation, *Journal of Atmospheric and Oceanic Technology*, **9,** 15–27.

BRUNEL, P., and MARSOUIN, A., 1987, An operational method using ARGOS for navigation of AVHRR imagery. *International Journal of Ren* 569–578.

CHISHOLM, J. S. R., 1973, Rational approximation defined from doubl *Mathematical Computations*, **27,** 841–848.

CLARK, J. R., and LAVIOLETTE, P. E., 1981, Detecting the movement of ocea registered TIROS-N imagery. *Geophysical Research Letters*, **8,** 229–2

CORNILLON, P., GILMAN, C., STRAMMA, L., BROWN, O., EVANS, R., and B Processing and analysis of large volumes of satellite derived therma *Journal of Geophysical Research*, **92,** 12 993–13 002.

CRACKNELL, A. P., and PAITHOONWATTANAKIJ, K., 1989, Pixel and sub-pi geometrical correction of AVHRR imagery. *International Journal of* **10,** 661–667.

EMERY, W. J., and IKEDA, M., 1984, A comparison of geometric correcti AVHRR imagery. *Canadian Journal of Remote Sensing*, **10,** 46–57.

EMERY, W. J., BROWN, J., and NOWAK, Z. P., 1989, AVHRR image navigation: summary and review. *Photogrammetric Engineering and Remote Sensing*, **55,** 1175–1183.

FRIEDMANN, D. E., FRIEDEL, J. P., MAGNUSSEN, K. L., KWOK, R., and RICHARDSON, S., 1983, Multiple scene precision rectification of spaceborne Imagery with very few ground control points. *Photogrammetric Engineering and Remote Sensing*, **49,** 1657–1667.

GUPTA, R. K., 1992, Processing error reduction factors in the generation of geometrically corrected NOAA/AVHRR vegetation index images. *International Journal of Remote Sensing*, **13,** 515–526.

HARROD, E. D., 1990, *NOAA/NESDIS polar data ingest and navigation. Proceedings of the North American NOAA Polar Orbiter Users Group, edited by D. Hastings, Second Meeting, 24–25 May 1990, New Carrollton, MD.*

KIRKHAM, R. G., and STEVENSON, M. R., 1976, Computer generated gridding of digital satellite imagery. *Remote Sensing of the Environment*, **5,** 215–224.

KLOSTER, K., 1989, Using TBUS orbital elements for AVHRR image gridding. *International Journal of Remote Sensing*, **10,** 653–659.

LEGECKIS, R., and PRITCHARD, J., 1976, Algorithm for correcting the VHRR imagery for geometric distortion due to the Earth curvature, Earth rotation and spacecraft roll attitude errors. NOAA Technical Memorandum NESS 77, NOAA/NESS, (Washington, DC: NOAA).

MALHOTRA, R. C., AND RADER, M. L., 1975, Locating remotely sensed data on the ground. In: *Remote Sensing. Energy-Related Studies*, edited by T. N. Veziroglu (New York: J. Wiley & Sons), pp. 431–436.

MARSOUIN, A., and BRUNEL, P., 1991, Navigation of AVHRR Images Using ARGOS or TBUS Bulletins. *International Journal of Remote Sensing*, **12,** 1575–1592.

MCCONAGHY, D. C., 1980, Geographic Location of Individual Pixels. *Remote Sensing of Environment*, **10,** 81–84.

O'BRIEN, D. M., and TURNER, P. J., 1992, Navigation of coastal AVHRR Images. *International Journal of Remote Sensing*, **13,** 509–514.

PRESS, W. H., FLANNERY, B. P., TEUKOLSKY, S. A., and VETTERLING, W. T., 1990, *Numerical Recipes* (Cambridge: Cambridge University Press).

SHARMA, OM P., 1990, Advanced Earth Location Data System (AELDS). SSAI report, Contract 50-DDNE-6-00009, SSAI, Seabrock, MD.

TORLEGARD, A. K. I., 1986, Some photogrammetric experiments with digital image processing. *Photogrammetric Record*, **12,** 175–186.